DENSIFICATION OF NANO-SIZED BORON CARBIDE

A Thesis
Presented to
The Academic Faculty

by

John Shupe

In Partial Fulfillment
of the Requirements for the Degree
Master of Science in the
School of Materials Science and Engineering

Georgia Institute of Technology
May 2009

DENSIFICATION OF NANO-SIZED BORON CARBIDE

Approved by:

Professor Robert Speyer, Advisor
School of Materials Science and Engineering
Georgia Institute of Technology

Professor Robert L. Snyder
School of Materials Science and Engineering
Georgia Institute of Technology

Professor Joe K. Cochran
School of Materials Science and Engineering
Georgia Institute of Technology

Date Approved: 7 January 2009

ACKNOWLEDGEMENTS

I would like to start by thanking my adviser Dr. Robert Speyer for his wisdom and guidance over the course of the last four semesters. His leadership has been invaluable to me and this project. Dr. Namtae Cho has been an excellent mentor and friend during my time at Georgia Tech, and I cannot thank him enough. I found his expertise to be my greatest resource. Additionally, I am most grateful to my colleagues in the lab who have helped me during my time as a graduate student, and without whom I would still be working on this Thesis.

I cannot thank my family enough for the care and support they have provided me with over the last year. Perhaps none have provided me with aid and encouragement as much as my fiance Leah who has endured much. Finally, I'd like to acknowledge my friends who are always there to remind me of what is truly important.

TABLE OF CONTENTS

LIST OF TABLES

LIST OF FIGURES

SUMMARY

Boron carbide nano-powders, singly-doped over a range of compositions, were pressurelessly-sintered at identical temperature and atmospheric conditions in a differential dilatometer to investigate sintering behavior. Samples that achieved relative densities greater than 93% of theoretical density were post-HIPed. Post-HIPing resulted in an increase in relative density as well as an increase in Vicker's hardness. To optimize the sintering behavior, nano-powders with multiple dopants were prepared based on the results of single dopant experiments. These powders were studied using the same heating schedule as the single dopant samples. The powder with optimized composition was selected, and 44.45 mm diameter disks were pressed to determine the effects of sample size.

Powder composition #166 with Al, Ti, W and Mg additions was processed using different methods in order to create defect-free green bodies after uniaxial pressing. The 44.45 mm diameter compacts were heat-treated to remove organics and B_2O_3 coatings on particles and then encapsulated in an evacuated fused silica ampule. Encapsulated samples were HIPed at temperatures below the coarsening region observed in the dilatometric traces of multiply-doped nano-powders. The E-HIPed sample showed a relative density of 96% with a limited extent of nano-sized grain microstructure.

CHAPTER I

INTRODUCTION

Boron carbide is a material of great interest to modern industry. Excellent hardness, fracture toughness, and Young's modulus make it an attractive material for wear applications and cutting tools [1]. Combined with its low specific gravity, boron carbide is ideal for personal body armor. Until recently boron carbide was difficult to densify using pressureless sintering due to the highly covalent nature of its bonding and low plasticity [2]. Commercially available boron carbide is hot pressed. Recent advancements in boron carbide powder production techniques have led to readily available powders with nano-sized particles. Recent work has been performed using pressureless sintering in an effort to study how nano-particle compacts can be densified [4].

The mechanical properties of ceramics tend to improve as porosity decreases. Hard ceramics such as boron carbide obey the Hall-Petch relationship which states that the strength of a material increases as the square root of the grain size decreases [5]. Therefore, it is advantageous to increase the relative density as well as create a finer grain microstructure. Pressureless sintering generally requires sintering aides in order to reach high relative densities [6]. Such additives are known to degrade mechanical properties [2]. Carbon is an important additive in boron carbide processing. Research devoted to sintering boron carbide with carbon additions has yielded relative densities of 98% [7]. Cho *et al.* have presented findings in which boron carbide was sintered to theoretical densities without the addition of sintering aides [8].

Previous work with boron carbide nano-powder within the same lab focused on applying techniques learned during research on d_{50}=0.8 μm powder and applying it to nano-powder [9]. The result was the identification of a phenomenon occurring during

sintering in which nano-particles melted at temperatures below boron carbide's bulk melting temperature. This effect was attributed to the lowering of the apparent melting temperature of the nano-particles due to their size as well as a further drop in apparent melting temperature due to the presences of carbon, which may have formed a eutectic. These melted regions were interpreted to grow in size, possibly taking on a spherical shape, as nano-particles melted and added to the region until it soldified. These regions impeded densification until higher temperatures. Lamellar regions then liquefied again upon further heating, causing rapid densification [8].

This thesis will present experiments and results from the pressureless sintering of nano-powders. Multiple dopants were added in varying concentrations in order to study their effect on sintering. This thesis presents follow up work to previous research. Some samples were hot isostatically pressed following sintering. Experiments were also conducted using encapsulated hot isostatic pressing.

CHAPTER II

THEORETICAL BACKGROUND

2.1 Boron Carbide

Boron carbide was first synthesized in 1883, and its chemical formula, B_4C, was assigned in 1934 [10]. With a Knoop hardness of ∼2800 kg/mm under a 100 g load, it is the third hardest material known to man after diamond and cubic boron nitride [1]. Boron carbide's excellent hardness and refractory nature derive from the highly covalent nature of its atomic bonds [7]. High mechanical strength and melting point make this material of interest for structural applications, while a low density gives it an advantage in applications in which weight is a critical factor. Additionally, boron carbide exhibits semiconductive as well as thermoelectric properties combined with high neutron absorption cross section [2]. Due to the ability of boron to substitute carbon in the lattice, it is now understood that boron carbide exists as a range possible compositions. The carbon-rich extreme of this composition range is associated with a $B_{4.3}C$ stoichiometry, while $B_{10.4}C$ represents the boron-rich limit as shown in Figure 2 [11]. Boron carbide obtained through commercial sources is assumed to be a B_4C composition.

Boron carbide with B_4C composition consists of a rhombohedral unit cell composed of eight $B_{11}C$ icosahedrons located at the corners of the unit cell and a three-atom chain along the main diagonal [2]. As the boron content of the solid solution is increased, the three-atom chain, initially of the configuration C-B-C, is substituted with C-B-B chains [11]. As the composition varies to less than 13.3 mol% C, $B_{11}C$ icosahedrons are replaced with B_{12} icosahedrons [12]. Variations in composition directly correlate to changes in the volume of the unit cell to the effect that excess

boron dilates the unit cell [2].

2.2 Green Processing

Uniaxial pressing is often used as a simple technique to form ceramic green bodies. A die and punch assembly is filled with loose powder. A hydraulic piston then applies a known load. Pressures of around 20-100 MPa are typically used. Ceramic powders are generally mixed with polymers. These polymers perform a variety of functions such as binding, plasticizing and lubricating. Binders give the green body handling strength while plasticizers permit binders to deform at room temperature, allowing for particle flow and increased packing. Lubricants reduce die friction effects, in turn decreasing packing gradients. Generally, a minimal amount of these additives is used to reduce gaseous combustion or decomposition products during burnouts that could otherwise bloat the green body. Loose powder with binder tends to have poor fill density in dies. Due to the general irregularity in shape between particles, there are substantial frictional forces that oppose packing. Several techniques can be applied to improve packing; however, for large-scale operations spray dried powder is preferred. Spray drying is a technique wherein powder, binder, plasticizer, lubricants, and deflocculants are mixed in a solvent and then sprayed. Droplets dry while falling, taking on spherical shapes. Spheres of bound powder can then flow or roll easily into the die, filling it uniformly. Uniaxial pressing works best for thin parts in which pressure gradients, occurring as a result of the frictional forces between the wall of the die are minimized [13]. For thicker or larger parts, cold isostatic pressing yields more uniform green bodies. Here the powder is loaded into a flexible mold. The mold and powder are then placed in a latex bag that is evacuated and sealed. The bag is then submerged in a mixture of oil and water and pressurized to $\sim$300 MPa. CIPing can also be used to eliminate density gradients in a uniaxially pressed sample or to improve its green density. The technique used for pressed green bodies is exactly the

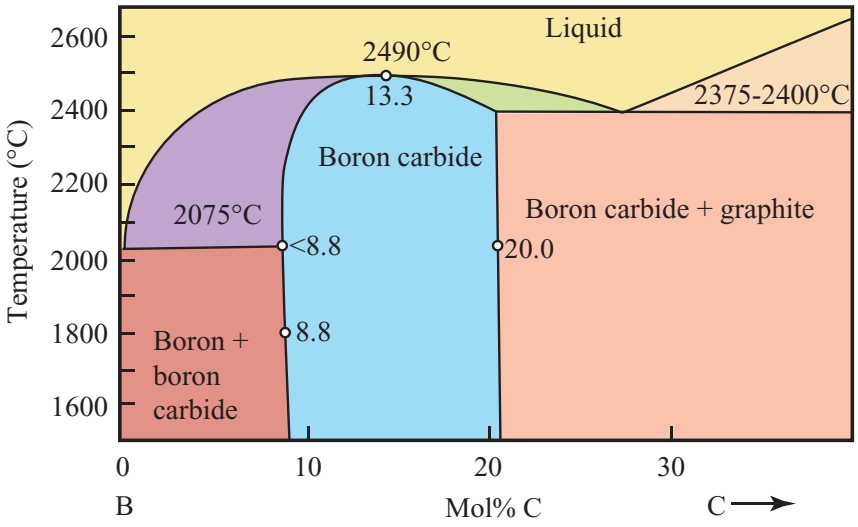

Figure 1: Boron carbide phase diagram [2].

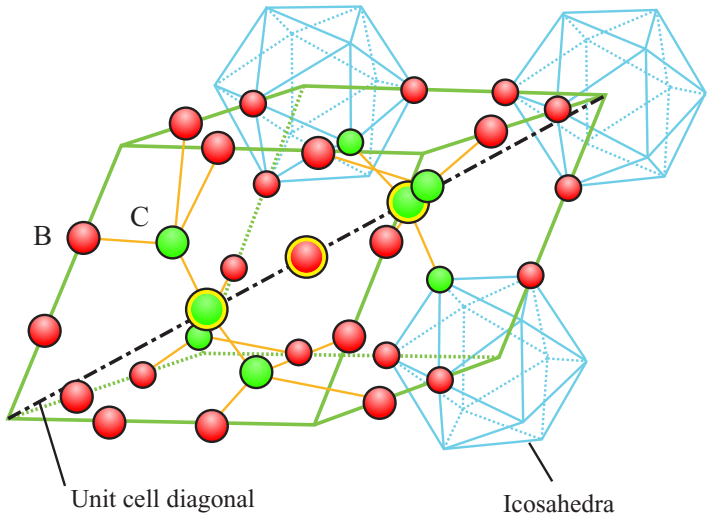

Figure 2: Crystal structure of B_4C [2].

same as for a mold except that the part is placed directly into the latex bag.

2.3 Sintering

Traditionally boron carbide has proven difficult to densify. Due to strong covalent bonding and lack of plasticity, high temperature and pressure are often necessary to achieve dense parts. Hot pressing, at temperatures around ∼2100°C and pressures of ∼30 Mpa, has been used with success [14, 3]. One of the limitations of hot pressing is the restriction on possible geometry. Complex, near-net shapes require other techniques such as pressureless sintering. However, due to the poor sintering results from pure boron carbide, sintering aides are used. Additives such as Al_2O_3, TiB_2, and W_2B_5 are often necessary to improve densification; however, these additives often have deleterious effects [15, 16, 17]. Additives that promote liquid phase sintering often lead to exaggerated grain growth as well as secondary phases at grain boundaries that weaken the material [2]. Carbon is the most widely used sintering aide. Schwetz and Vogt observed that the addition of carbon by in situ pyrolysis of phenolic resin to B_4C allowed densification up to 98% theoretical density [18]. Later work by Schwetz and Grellner focused on the microstructure of carbon-doped boron carbide and concluded that the presence of carbon retarded the surface and vapor transport mechanisms that normally inhibited densification [19]. Lee *et al.* showed that the presence of B_2O_3 facilitated a coarsening reaction between ∼1800°C and 2000°C [20]. By eliminating the B_2O_3 on the surface, relative densities of approximately 95% were achieved. Work by Cho *et al.* expanded on pressureless sintering by post-hot isostatic pressing sintered parts to theoretical density [8].

Due to innovations in powder synthesis, recent research has been conducted into the pressureless sintering of nano-powders. It has been hypothesized that the increased surface area and shortened diffusion distances of nano-powders would lead to an increase in the driving force for sintering [21, 22]. Previous work with pressureless

sintered metal oxide ceramic nano-powders has yielded promising results. Starting with an average particle size of 50 nm, samples reached 95% theoretical density [23]. Previous work by Cho *et al.* has shown that a process in competition with sintering, identified as nano-melting, reduces the driving force for sintering [8]. Continuing research by Cho *et al.* has yielded samples of 95% theoretical density, despite the nano-melting phenomenon [9]. This thesis presents research into dopants that improve densification through pressureless sintering and post hot isostatic pressing.

2.4 Encapsulated HIP

Encapsulated hot isostatic pressing is a technique that can be used to create complex-shaped, dense parts out of materials otherwise difficult to densify. High-precision dense parts have been successfully created from Si_3N_4, normally a difficult material to densify, using this technique [24]. The first step in encapsulated HIPing is sealing a porous body in a material such as glass or metal under vacuum. The encapsulated part is then placed in a HIP and heated in an inert atmosphere. The glass or metal is selected such that the material softens before the desired sintering temperature. Once the encapsulating material reaches it's softening point, a pressure of $\sim$200 MPa is applied. At the hold temperature, the applied pressure causes an increase in the driving force for densification, resulting in increased relative density. Parts with no open porosity are considered self-encapsulated. Parts with density greater than $\sim$93-95% are considered to have no open porosity [24]. It may be possible to HIP self-encapsulated samples to improve their density. This process is sometimes referred to as post-HIPing because a different technique is needed to eliminate open porosity prior to the HIPing.

CHAPTER III

EXPERIMENTAL PROCEDURE

3.1 Sintering Optimization

3.1.1 Sample Preparation

As-received boron carbide nano-powders (PPG industries, Inc., Pittsburgh, PA) with a size range of 20 - 40 nm were mixed with methanol, and the suspension was sonicated (FS-14 solid state ultrasonicator, Fisher Laboratory Equipment Division, Pittsburgh, PA) for 5 minutes. The suspensions were dried in a 70°C oven for 12 h. This process was repeated three times to eliminate excess boron oxide from particle surfaces.

Methanol-washed powder was placed in a die and punch assembly (Model No. 3925, Carver, Inc., Wabash, IN) and pressed at 300 MPa to produce powder compacts with a green density greater than 60% of theoretical in the form of cylindrical pellets, 6.44 mm in diameter and ∼5 mm in height. Powder prepared by various methods was uniaxially pressed at 40 MPa, (Model No. 3925, Carver Inc. Wabash, IN) into cylindrical disks 44.45 mm in diameter and ∼5 mm in height. Compacts were CIPed in evacuated latex gloves at 300 MPa for 5 min.

3.1.2 Sintering

All samples were sintered in a dilatometric furnace (1000-2560 FP, Thermal Technology, Inc., Santa Rosa, CA). The dilatometer (Theta Industries, Inc., Port Washington, NY) uses a double-pushrod system in a graphite casing (Poco Graphite Inc., Decatur, TX) that extends into the furnace. A linear variable differential transformer (LVDT) position transducer measures dimensional changes of the sample relative to the graphite reference. A counterweight was used to avoid any particle sliding within the powder compacts that might result from the force of the pushrod. Temperature

was monitored via an infrared pyrometer (MAISC, Raytek Co., Santa Cruz, CA) sighted on the samples through the graphite casing. Measurement at a wavelength of 1.0 μm was conducted through a fused silica viewing port mounted on the side wall of the furnace. Calibration of the pyrometer was based on the allotropic transformation of a pressed compact of high-purity iron (99.99%, Sigma-Aldrich, St. Louis, MO), the polymorphic transformation of high-purity ZrO_2 (99.99%, Sigma-Aldrich, St. Louis, MO), and direct comparison with a W-Rh thermocouple up to 1900°C.

After evacuating the furnace and backfilling with helium two times, samples were heated under flowing helium (5.7 ℓ/h) to 2300°C at 10°C/min and soaked at this temperature until the shrinkage rate was less than 0.005%/min. After cooling at 50°C/min to room temperature in helium, geometrical and Archimedes densities were obtained.

After pressureless sintering, specimens with greater than 93% relative density were hot isostatically pressed (i.e. post-HIPed, American Isostatic Presses, Inc., Columbus, OH) using a heating rate of 20°C/min to 2150°C, soaked for 125 minutes in Ar at 69-310 MPa, and cooled at 20°C/min to room temperature. Pressure was applied gradually during heating with target values achieved just before the 2150°C soak. Temperature and pressure were both maintained through the soak after which furnace power was turned off, and pressure and temperature reduced concurrently.

3.1.3 Characterization

Specimen densities were measured using Archimedes method. Percent relative densities were calculated based on the density of stoichiometric B_4C (2.52 g/cm^3). The dry weight (W_1) of each sample was measured just after sintering. The sample was then boiled in deionized water for more than 1 h and cooled to room temperature. The immersed weight in water (W_2) was measured at room temperature in deionized

water. Finally, the water-impregnated weight (W_3) was measured. Five measurements were made for each sample, and the mean values were recorded. The density ρ was calculated from:

$$\rho = \frac{W_1 \cdot \rho_w}{W_3 - W_2}$$

where ρ_w is the density of water (g/cm^3), which changes slightly with temperature.

$$\rho_w = 1.0017 - 0.0002315T$$

where T is equal to the water temperature in °C. The total porosity P (in percent) of the samples was calculated by the following equation:

$$P = 100 \cdot \frac{\rho_{th} - \rho}{\rho_{th}}$$

where ρ_{th} is the theoretical density of the sample.

Densified specimens mounted in resin (Specifix 40, Struers, Westlake, OH) were successively ground using 45, 15, and 9 μm diamond grinding discs (Metal-bonded diamond grinding discs, Buehler, Lake Bluff, IL and Metadi Supreme II, Buehler, Lake Bluff, IL) with water. The grinding times and rotating speeds were ∼10 min and 150 rpm, respectively. Specimens were then polished with 3 and 1 μm diamond suspensions (Metadi Supreme II, Buehler, Lake Bluff, IL) on soft cloths (Texmet 1000, Buehler, Lake Bluff, Il). The polishing times and speeds were 60-120 min and 150 rpm, respectively. Specimens were rinsed with deionized water between each step.

Polished samples were electrolytically etched for 1 min in a solution of 1% KOH, using 0.03A/cm^2, applied using a current-source meter (Model 2400, Keithley, Taunton, MA). The microstructures of etched specimens were characterized using scanning electron microscopy (SEM, Model 1530, LEO Electron Microscopy, Inc., Oberkochen, Germany).

Indentation hardness values of polished specimens were measured using a Vickers indenter (Druamin 2, Struers, Westlake, OH) following the ASTM C1327-99 standard

test method for advanced ceramics; specimens were indented with a 9.81 N load for 15 s at multiple locations until ten acceptable (as specified in the standard test method) indents were obtained. Calibration of the indenter system was performed using a WC-bast NIST standard reference material (SRM No. 2831).

The phase identification was done using X-ray diffraction (PANalytical XPert PRO X-ray diffractometer, Natick, MA) with a scan speed of 1 s/step and a step size of 0.005° from 10 to 85° 2θ. All XRD peaks were obtained from near the surface after excess carbon was eliminated.

3.2 Encapsulated HIP

As-received PPG #166 nano-powder was uniaxially pressed and CIPed into 44.46 mm diameter disks as previously described. The compacts were then heat-treated at 1350°C for 12 h under vacuum to remove residual B_2O_3. After heat treatment, green body dimensional densities were measured. The powder compacts were then placed at the base of a closed-ended fused silica tube (45 mm in diameter) beneath fibrous fused silica felt. The tube was then evacuated to $\sim 1 \times 10^{-5}$ torr. The center of the tube, ~5 cm away from the sample, was sealed under vacuum by an oxy-hydrogen torch. The encapsulated sample was placed in the HIP (AIP6-30H Hot Isostatic Press, American Isostatic Presses, Inc., Columbus, Ohio). The temperature/pressure schedule is depicted in Figure 3.

After EHIP, surface silica was removed by grinding using sand paper and a glass bead-blaster. The Archimedes densities were measured based on the theoretical density of stoichiometric B_4C (2.52 g/cm^3). The phases present after EHIP were characterized by XRD after the surface was ground away (PANalytical X?ert PRO X-ray diffractometer, Natick MA). Indentation hardness values of polished specimens were measured using a Vickers indenter (Duramin-2, Struers, Westlake, OH) following the

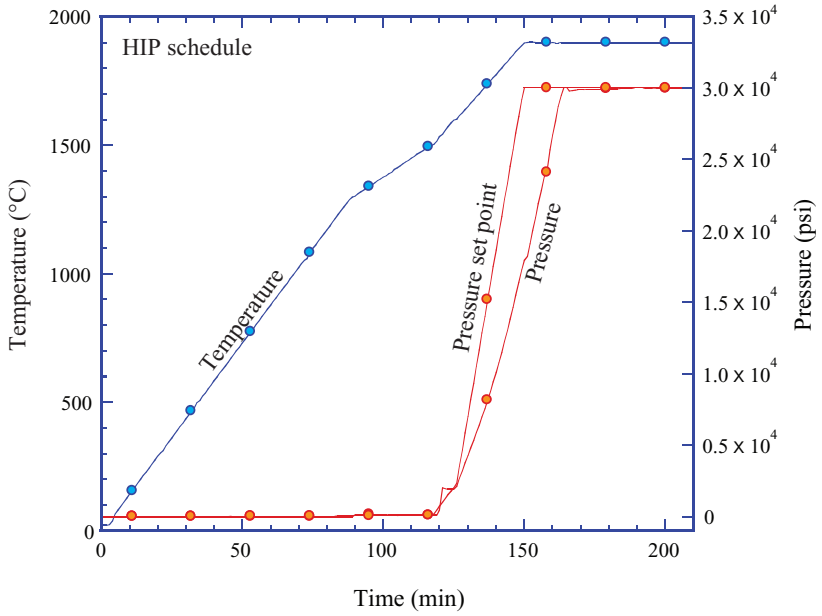

Figure 3: Heating and pressure schedule for EHIP. The sample was heated to 1900°C at 10°C/min in an Ar atmosphere. The pressure was increased starting at 1500°C to a value of 30000 psi at 1900°C.

ASTM C1327-99 standard test method for advanced ceramics; specimens were indented with a 9.81 N load for 15 s at multiple locations until ten acceptable indents were observed. Specimens were polished and etched for observation in a scanning electron microscope (SEM, LEO 1530, Carl Zeiss MicroImaging, Inc., Thornwood, NY) and an optical microscope (Olympus, BX40, Center Valley, PA).

CHAPTER IV

RESULTS

4.1 Powder Study based on Dopant

4.1.1 Al-doped Powder

The compositions of Al-doped powders are shown in Table 1.

Table 1: Powder description of Al-doped nano-powders

Sample Code	Description
PPG - 117	0.10 wt% Al-doped
PPG - 118	0.25 wt% Al-doped
PPG - 119	0.50 wt% Al-doped
PPG - 120	0.75 wt% Al-doped
PPG - 121	1.00 wt% Al-doped
PPG - 122	1.50 wt% Al-doped

Phase identifications of as-received Al-doped powders were preformed using X-ray diffraction, the results of which are shown in Figure 4. Boron carbide was detected as the main phase with graphite as a secondary phase in all as-received Al-doped powders. No Al compounds were detected, and some peaks from unknown phases were detected at $\sim$19° and $\sim$28° 2θ.

The green body densities after uniaxial pressing were measured geometrically using sample dimensions and dry weights. After sintering with the standard heating schedule, the dimensional and Archimedes densities were measured. The weight losses were calculated based upon the differences in weight before and after sintering. All relative densities and weight loss results are shown in Table 2. Initially, green body densities decreased until the amount of dopant exceeded 0.75 wt%, at which point density began to increase. The Archimedes relative densities after sintering did not show a clear trend with increasing dopant content. There were significant differences

between geometrical densities and Archimedes densities due to deformation during sintering.

Table 2: Relative densities and weight losses of Al-doped nano-powders.

Sample number	Green density (%)	Geometrical density (%)	Archimedes density (%)	Weight loss (%)
PPG #117	70.04	84.37	90.50	9.17
PPG #118	65.12	79.10	86.43	14.32
PPG #119	68.78	87.21	91.62	0.95
PPG #120	66.13	71.38	86.45	10.82
PPG #121	70.06	74.05	84.54	18.06
PPG #122	70.09	79.59	90.17	18.71

The dimensional changes of Al-doped nano-powders during sintering are shown in Figure 5. All Al-doped nano-powders underwent two-stage sintering. Small humps in the trace were observed at ∼1300°C, corresponding to the evaporation of residual B_2O_3. The sintering onset temperatures were higher, and the slopes of dimensional changes from the onset of sintering to the beginning of nano-melting became steeper with increased Al content. Decelerations in shrinkage, resulting from particle coarsening by nano-melting, were observed from 1850 to 2200°C. Slopes within this range tended to be steeper as Al concentration increased. After the plateau, the shrinkage rate re-accelerated up to the 2300°C soak. The net dimensional change increased as the amount of Al increased, except for the 1.50 wt% doped sample.

4.1.2 Y-doped Powder

Compositions of Y-doped nano-powders are shown in Table 3.

Table 3: Powder descriptions of Y-doped nano-powders.

Sample Code	Description
PPG #110	0.5 wt% Y-doped
PPG #111	2.0 wt% Y-doped
PPG #112	5.0 wt% Y-doped

The phase identifications of as-received Y-doped powders were performed using

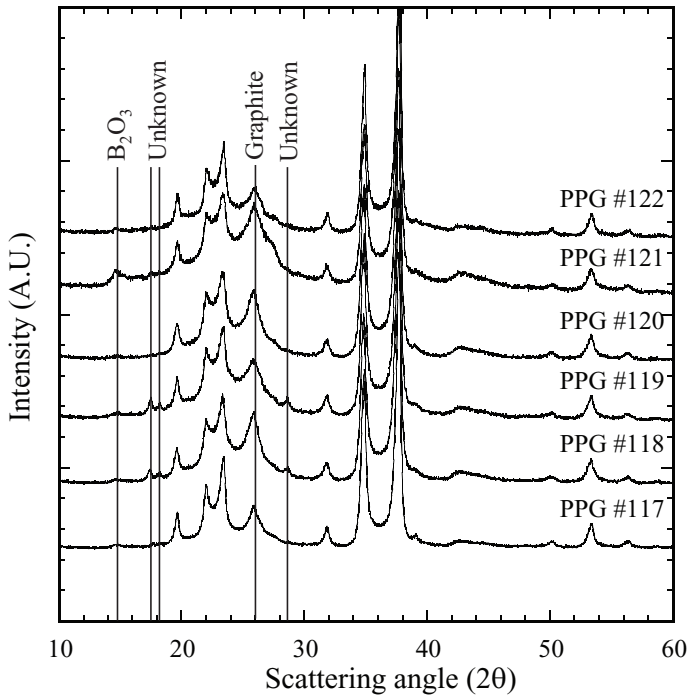

Figure 4: XRD peaks of Al-doped nano-powders.

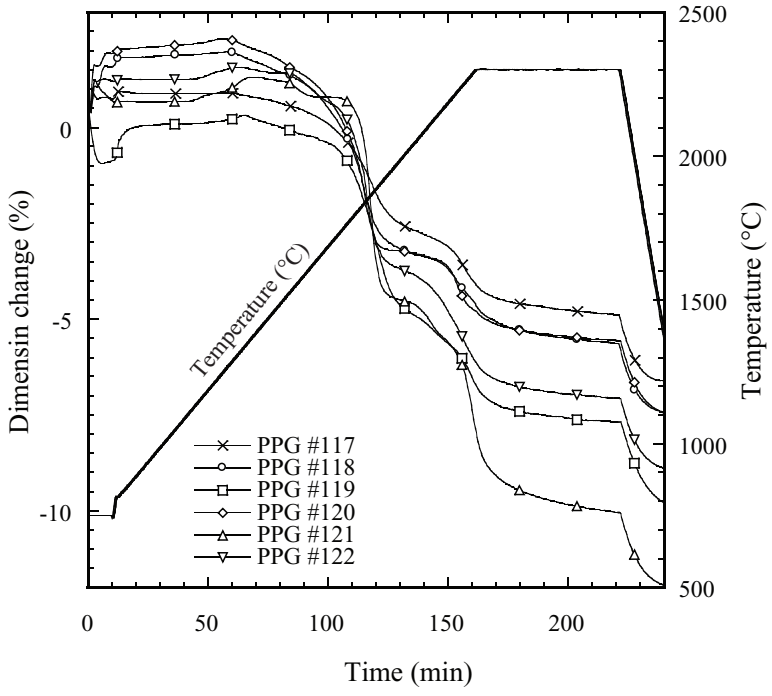

Figure 5: Dilatometry traces of Al-doped nano-powder compacts. The powder compacts were heated at 10°C to 2300°C in a He atmosphere and held for 1 h.

X-ray diffraction, and the results are shown in Figure 6. Boron carbide was detected as a primary phase with graphite as a secondary phase in all as-received Y-doped powders. As the amount of Y increased, YBO_3, B_2O_3 and graphite peaks increased in relative intensity, and an unknown phase was detected at $\sim 18^\circ$ 2θ in the case of 0.5 wt% doped powder.

All density and weight loss results are shown in Table 4. The green body densities and Archimedes densities showed decreasing trends as dopant concentration increased.

Table 4: Densities and weight losses of Y-doped nano-powders.

Sample number	Green density (%)	Geometrical density (%)	Archimedes density (%)	Weight loss (%)
PPG #110	69.89	83.28	89.45	6.75
PPG #111	69.35	83.88	89.08	8.75
PPG #112	66.26	79.76	86.08	8.81

The dimensional changes of Y-doped nano-powders during sintering are shown in Figure 7. All Y-doped nano-powders showed a two-stage sintering behavior. After the first humps, sintering onset temperatures decreased slightly with increasing Y content. The 5.0 wt% Y-doped sample showed a second expansion at $\sim 1700^\circ$C before sintering onset. The onset of nano-melting for each powder composition shifted to higher temperatures, and the widths and slopes of the nano-melting regions became narrower and flatter with increased Y content. All samples showed expansions near 2150°C and redensified at 2300°C. The net dimensional changes increased as the concentrations of Y increased.

4.1.3 La-doped Powder

Compositions of the La-doped powders are shown in Table 5.

Boron carbide was detected as the primary phase with graphite as a secondary phase in all as-received La-doped powders, as shown in Figure 8. LaB_6 was detected

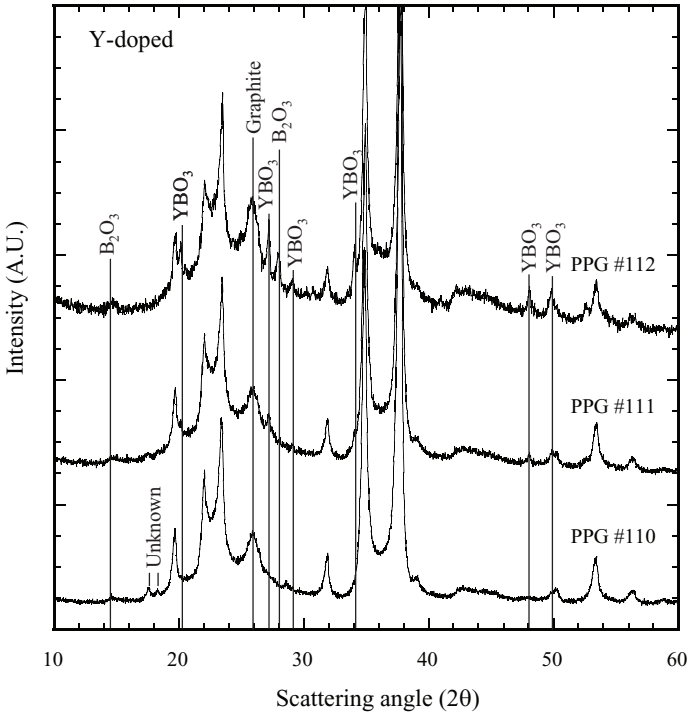

Figure 6: XRD peaks of Y-doped nano-powders.

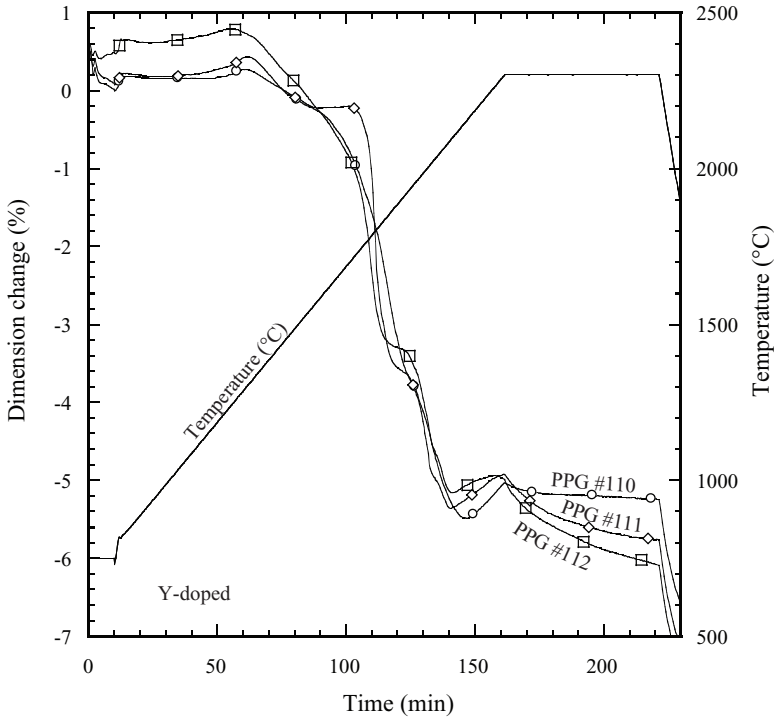

Figure 7: Dilatometry traces of Y-doped nano-powder compacts. The powder compacts were heated at 10°C/min to 2300°C in a He atmosphere and held for 1 h.

Table 5: Powder descriptions of La-doped nano-powders.

Sample Code	Description
PPG-146	0.1 wt% La-doped
PPG-147	0.5 wt% La-doped
PPG-148	2.0 wt% La-doped
PPG-149	4.0 wt% La-doped

as another secondary phase, and the peak heights increased as the concentration of La decreased. The background to signal ratio showed an increasing trend due to the decreased crystallinity of the La-doped B_4C powders.

All density and weight loss results of La-doped powders are shown in Table 6. The green body densities increased slightly with increased La concentration. The disparity between geometrical densities and Archimedes densities is due to nonuniform shrinkage in the samples during sintering. Geometrical density is calculated assuming a cylindrical shape to the pellets as a reference, which was inaccurate after sintering caused the part to assume a more complex shape. The 4.0 wt% doped powder showed a relative density of ∼70%. As the amount of La increased, Archimedes relative densities and weight losses increased; 4.0 wt% doped powder showed 94.66% relative density after sintering with 10.95% weight loss.

Table 6: Relative densities and weight losses of La-doped nano-powders.

Sample number	Green density (%)	Geometrical density (%)	Archimedes density (%)	Weight loss (%)
PPG #146	69.82	88.41	85.88	4.18
PPG #147	69.83	85.51	90.58	4.51
PPG #148	68.79	-	-	-
PPG #149	70.50	79.07	94.66	10.95

The dimensional changes from the onset of sintering to the beginning of nano-melting, as shown in Figure 9, decreased with increasing La content; however, after nano-melting, the trend reversed. The net dimensional changes increased as the concentration of La increased. The shifting of onset temperatures of the nano-melting

region was not observed in the La-doped powders.

4.1.4 Nb-doped Powder

Table 7 shows the compositions of Nb-doped nano-powders.

Table 7: Powder descriptions of Nb-doped nano-powders.

Sample Code	Description
PPG-150	0.5 wt% Nb-doped
PPG-151	2.0 wt% Nb-doped
PPG-152	5.0 wt% Nb-doped

NbB_2 was detected as a secondary phase in addition to graphite, and peak heights increased as the amount of Nb increased. In the case of the 0.5 wt% doped powder, a small amount of residual B_2O_3 was detected. All density and weight loss results are shown in Table 8. The green body densities tended to increase based on the concentration of dopant. Archimedes densities increased to ∼95% in the cases of 2.0 wt% and 5.0 wt% doped powders. The weight losses were ∼5% and increased slightly as dopant content increased.

The dimensional changes of Nb-doped nano-powders are shown in Figure 11. All Nb-doped nano-powders showed a two-stage sintering behavior which is typical of nano-sized powder. Sintering onset temperatures decreased slightly with increasing Nb content. The dimensional changes before nano-melting increased, and the slopes during nano-melting became steeper as the amount of Nb increased. No shift in the nano-melting region was observed, and the net dimensional changes increased with increasing Nb content.

Phase changes during sintering were identified using X-ray diffraction and are shown in Figure 12. The peak widths decreased due to the particle coarsening during sintering. There were no phase changes after sintering compared to as-received powders, and the peak heights of NbB_2 increased as the concentration of Nb increased.

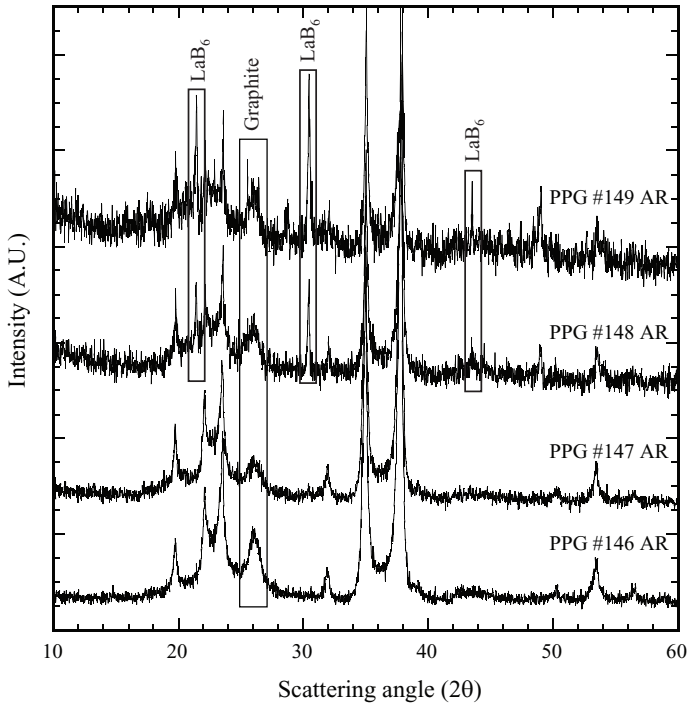

Figure 8: XRD peaks of La-doped nano-powders.

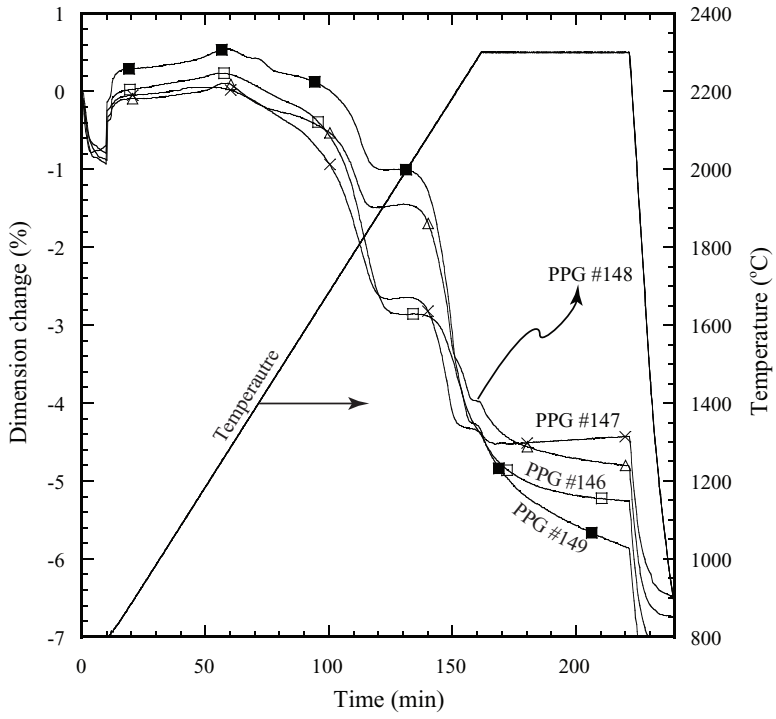

Figure 9: Dilatometric traces of La-doped nano-powders. The powder compacts were heated at 10°C/min to 2300°C in a He atmosphere and held for 1 h.

Table 8: Densities and weight losses of Nb-doped nano-powders.

Sample number	Green density (%)	Geometrical density (%)	Archimedes density (%)	Weight loss (%)
PPG #150	68.84	86.13	90.12	5.00
PPG #151	71.93	93.45	94.97	5.48
PPG #152	70.14	91.40	94.90	5.60

However, the peak height of carbon ($\sim$26° in 2θ) decreased.

4.1.5 B-rich Al-doped Powder

The sintering behavior and properties of multiply-doped nano-powders were investigated. Table 9 shows the compositions of B-rich B_4C powders doped with different amounts of Al.

Table 9: Powder descriptions of B-rich Al-doped nano-powders.

Sample Code	Description
PPG-153	$B_{6.8}C$, without Al, (B-rich exp)
PPG-154	$B_{3.9}C$, 0.39 wt% Al, (B-rich exp)
PPG-155	$B_{4.2}C$, 0.30 wt% Al, (B-rich exp)
PPG-156	$B_{5.2}C$, 0.19 wt% Al, (B-rich exp)

No Al compounds were detected by X-ray diffraction, as shown in Figure 13. Except for pure B-rich powder, the heights of graphite peaks decreased slightly as Al content increased. All density and weight loss results are shown in Table 10. The green body densities decreased as dopant content increased, except for pure B-rich powder, which showed 63.08% green body density. After sintering, the Archimedes densities decreased with increasing Al content, while weight losses increased.

The dimensional changes of B-rich, Al-doped nano-powders are shown in Figure 14. All B-rich Al-doped nano-powders showed a two-stage sintering behavior,

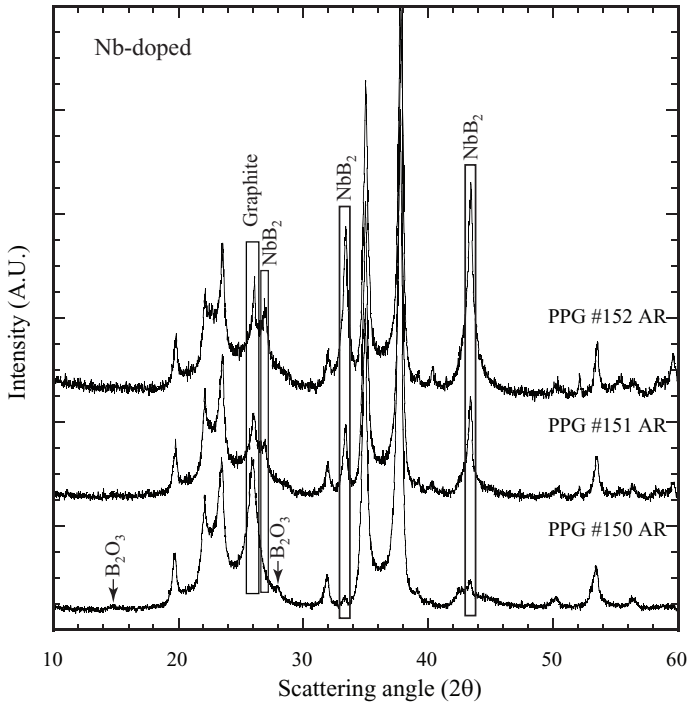

Figure 10: XRD peaks of Nb-doped nano-powders.

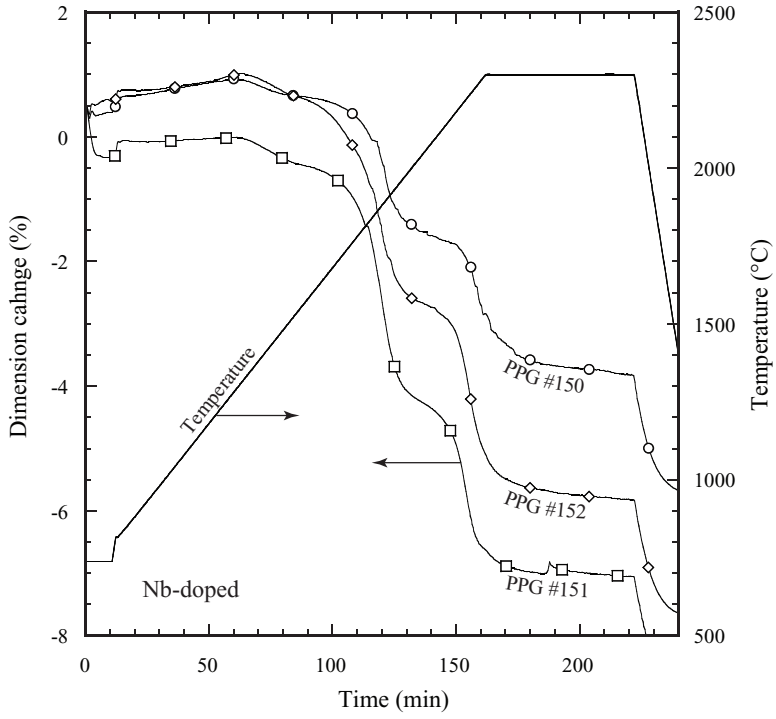

Figure 11: Dilatometric traces of Nb-doped nano-powdercompacts. The powder compacts were heated at 10°C/min to 2300°C in a He atmosphere and held for 1 h.

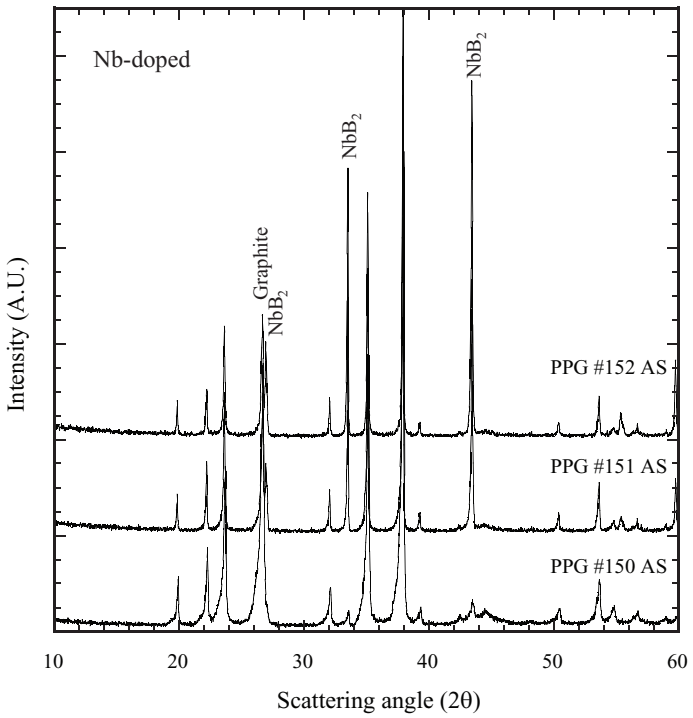

Figure 12: XRD peaks of Nb-doped nano-powders after sintering.

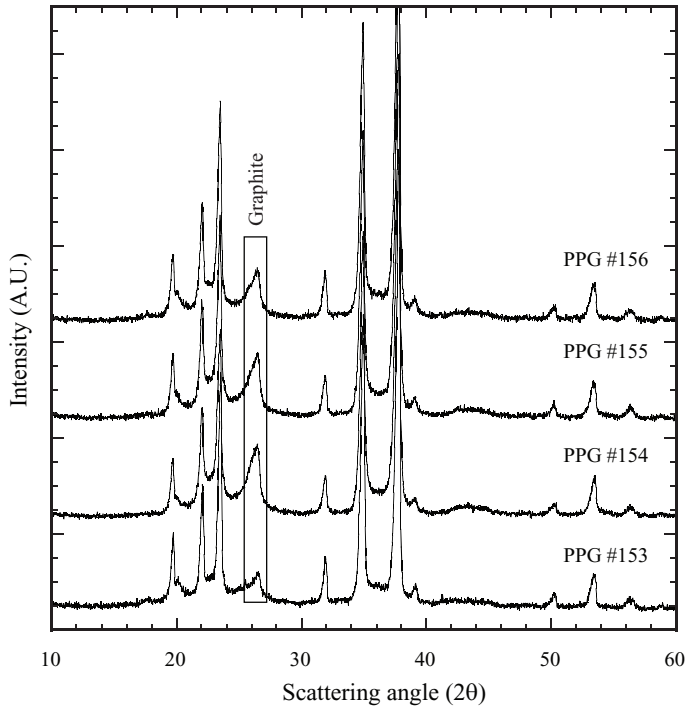

Figure 13: XRD peaks of B-rich nano-powders doped with Al

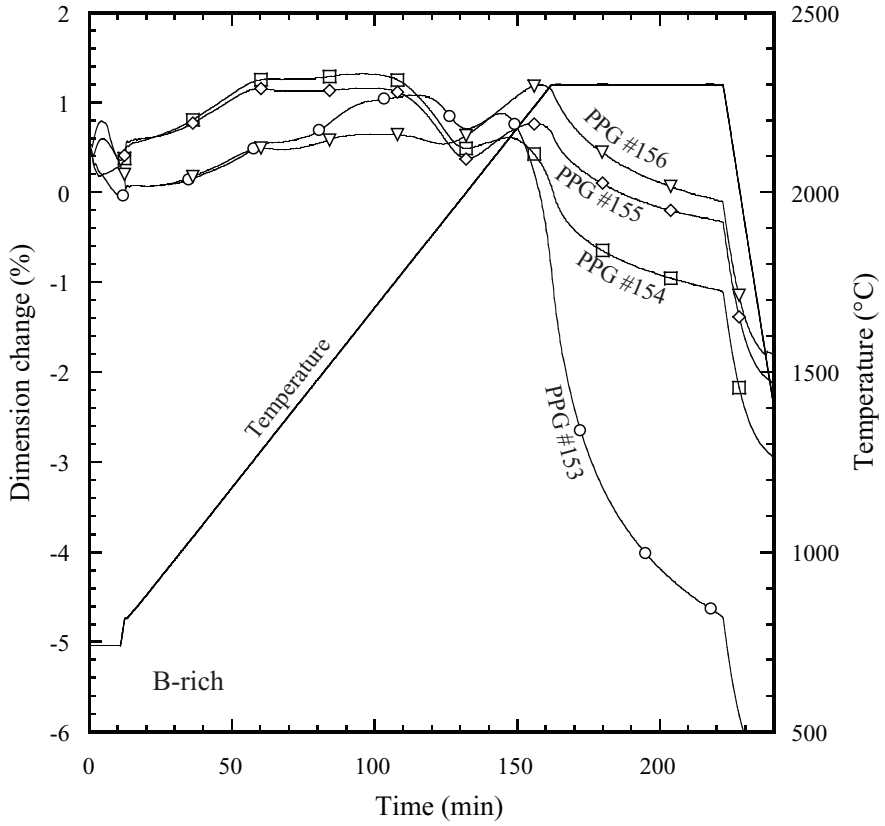

Figure 14: Dilatometric traces of B-rich Al-doped nano-powder compacts. The powder compacts were heated at 10°C/min to 2300°Cin a He atmosphere and held for 1 h.

Table 10: Densities and weight losses of B-rich Al-doped nano-powders.

Sample number	Green density (%)	Geometrical density (%)	Archimedes density (%)	Weight loss (%)
PPG #153	63.08	69.57	72.16	8.90
PPG #154	70.36	76.82	77.67	6.50
PPG #155	68.54	71.50	72.12	7.32
PPG #156	68.23	68.30	68.76	8.08

which is typical of nano-sized powders. All B-rich powders showed a positive dimensional change until ∼1800°C. Samples then began to sinter until an expansion at 1900°C, followed by continued sintering. The sintering onset temperatures and net dimensional changes decreased as the concentration of Al increased.

4.2 Post-HIPing

After post-HIPing, the relative densities and hardness values were significantly enhanced. The results are shown in Table 11. After pressureless sintering, samples were ~95% of their theoretical density, with Vickers hardness values greater than 2100 Kg/mm^2. The post-HIPing process increased both the relative density and hardness. In the case of the 2.0 wt% W-doped sample, density increased up to 98.45% of theoretical density, and hardness increased concurrently.

Table 11: Densities and hardness values before and after HIPing.

Sample Code	Composition	Before HIP		After HIP	
		Relative density (%)	Hardness	Relative density (%)	Hardness
PPG #91	0.5 wt% Al-doped	94.67	2483 ± 87	96.22	2560 ± 108
PPG #100	3.0 wt% Ti-doped	94.68	2289 ± 108	97.10	2558 ± 328
PPG #103	5.5 wt% Zr-doped	93.50	2044 ± 280	94.88	2309 ± 415
PPG #108	2.0 wt% W-doped	95.15	2170 ± 120	98.45	2722 ± 130
Stark HS	Undoped	96.70	2650 ± 100	99.10	2900 ± 110

No phase changes were observed in the cases of Al-doped and Ti-doped samples after HIPing, as seen in Figure 15. In the case of the Zr-doped sample, ZrC was detected as a new phase. The W-doped sample showed minor peak height changes between WB_2 and W_2B_5 phases, while SiO_2 peaks disappeared after HIPing.

The microstructures of post-HIPed samples were observed using SEM after electrochemical etching. All samples showed different microstructures based on dopants. Figure 16 shows the microstructures of samples at low magnification. The Al-doped sample showed a homogeneous distribution of small sized B_4C and graphite phases without large pores. However, in the case of the Ti-doped sample, relatively large pores were observed. The Zr-doped sample showed an average grain size of ~30 μm, with pores within grains and at grain boundaries. The W-doped sample showed both homogeneous and small B_4C grain sizes with large graphite regions.

SEM micrographs at higher magnification are shown in Figure 17. The Al-doped

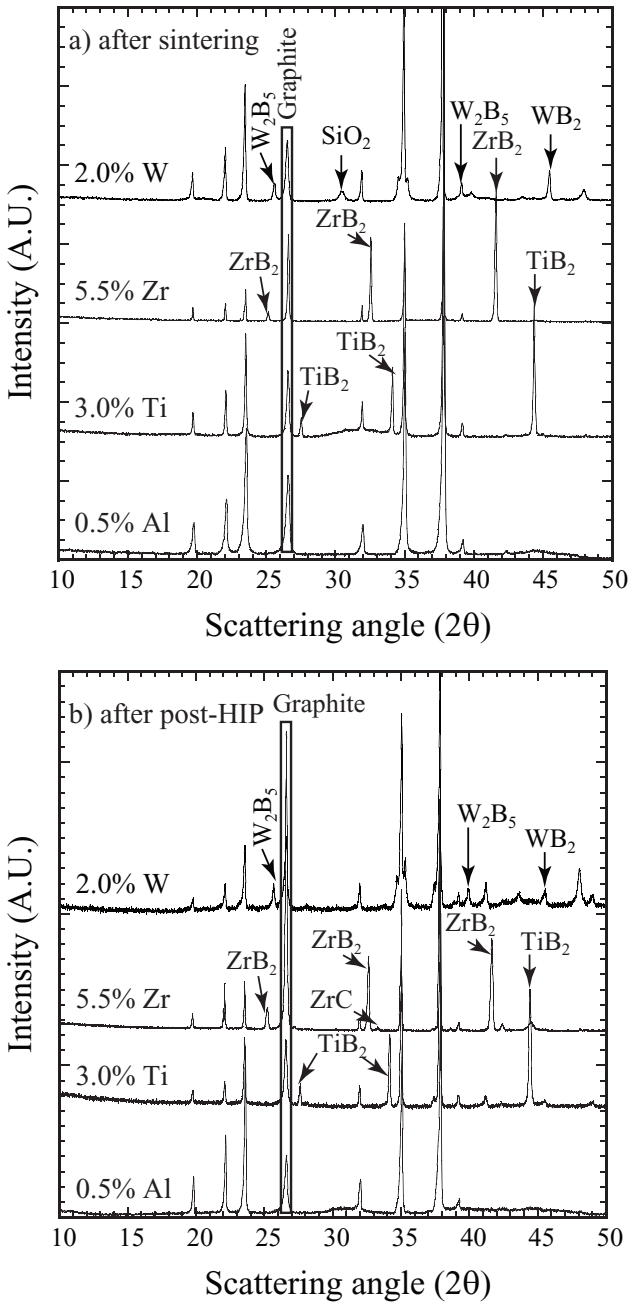

Figure 15: XRD peaks of a) post-pressurelessly sintered samples and b) post-HIPed samples.

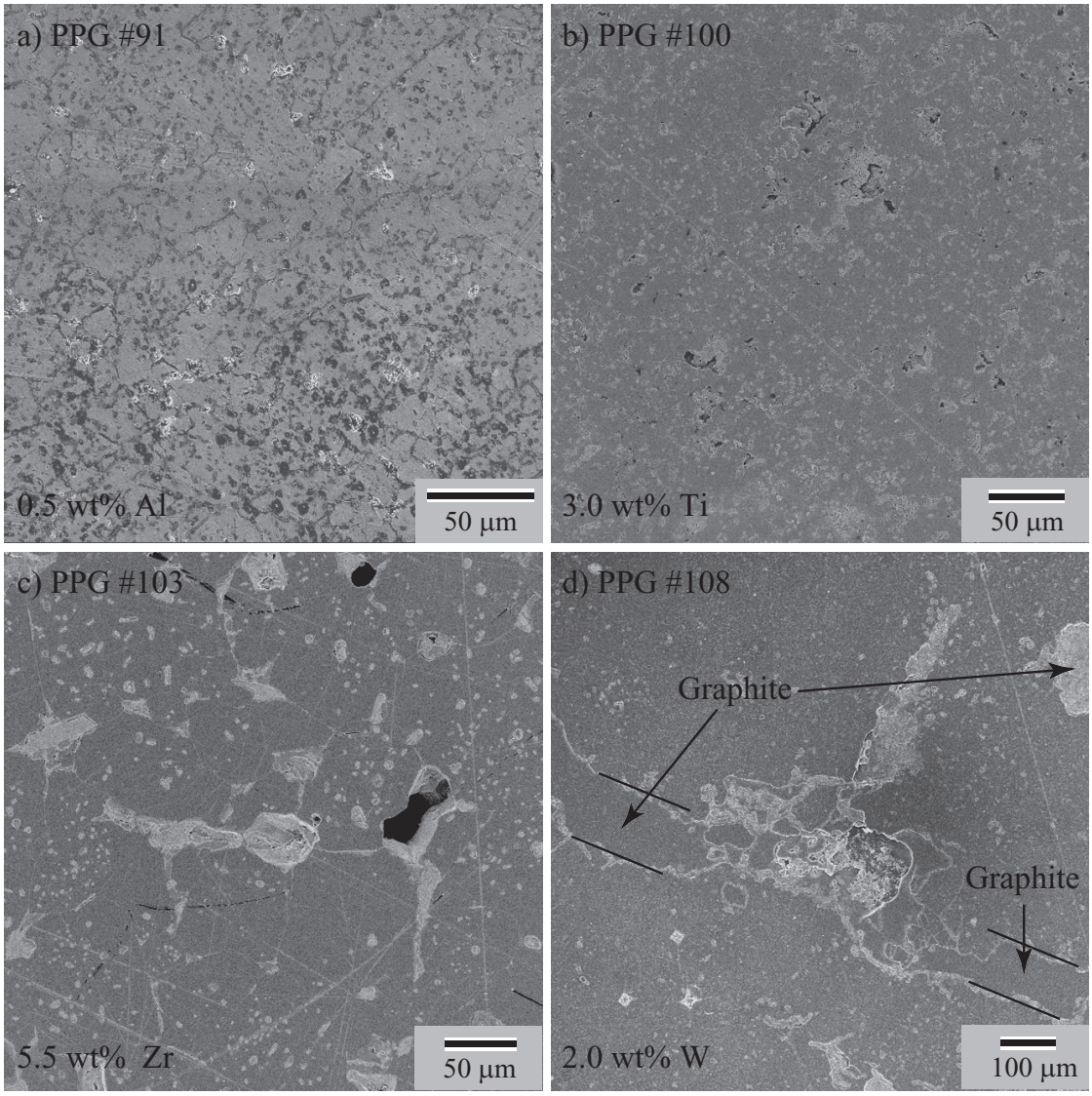

Figure 16: SEM micrographs of post-HIPed samples at low magnification a) 0.5 wt% Al b) 3.0 wt% Ti c) 5.5 wt% Zr and d) 2.0 wt% W doped samples.

specimen showed a homogeneous microstructure with B_4C and graphite. The Ti-doped sample showed a graphite phase within the grains and at grain boundaries, while the TiB_2 phase was observed only at grain boundaries. In the Zr-doped sample, the graphite phase was observed inside of grains and at grain boundaries, while the ZrB_2 phase was observed at grain boundaries only. The WB_2 and graphite phases were observed at the grain boundaries of the W-doped sample.

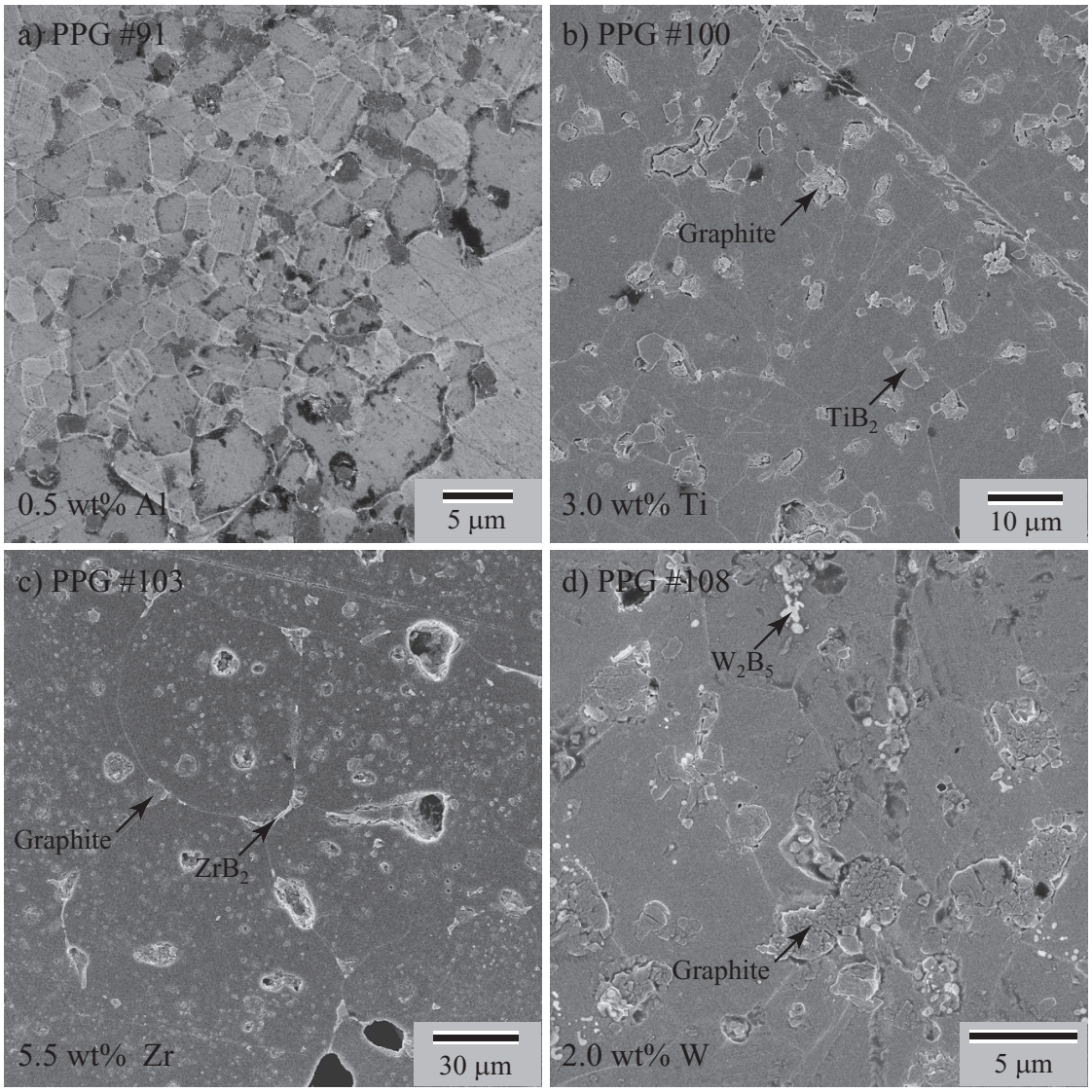

Figure 17: SEM micrographs of post-HIPed samples a) 0.5 wt% Al b) 3.0 wt% Ti c) 5.5 wt% Zr and d) 2.0 wt% W doped samples.

4.3 Optimization for Scaling-up

Based on the sintering behaviors of doped nano-powders, various multiply-doped nano-powders were investigated for scaling-up. Compositions, green processing, and sintering schedules were optimized.

4.3.1 Multiply-doped Powder

Table 12 shows the compositions of multiply-doped nano-powders. In this series, nano-powders were doped with different amounts of Al, Ti, W and Mg. Densities and weight losses were measured after pressureless sintering with a standard heating schedule.

All powders were pressed into pellets 6.44 mm in diameter and ∼5 in mm height. Samples were set in a B_4C crucible and heated to 2300°C with a constant heating rate of 10°C/min and held at that temperature for 1 h. The green and Archimedes densities and weight losses are shown in Table 13.

Nano-powder that was doped with 0.1 wt% Al, 0.5 wt% Ti, 0.1 wt% W and 0.5 wt% Mg (PPG #134) showed the highest relative density (95.42%) and relatively low weight loss. Based on the results of PPG #134 powder, minor changes in compositions were investigated and described in Table 14.

All small pellets with 6.44 mm diameters were set in a B_4C crucible, heated to 2300°C, and held at that temperature for 1 h. The green and Archimedes densities and weight losses are shown in Table 15. Nano-powders doped with 0.1 wt% Al, 0.5 wt% Ti, 0.1 wt% W and different concentrations of Mg, corresponding to PPG #166 to #168, showed ∼95% relative density after sintering.

4.3.2 Heating Schedule Optimization

Small pellets with 6.44 mm diameters were used for heating schedule optimization. The sintering behaviors of samples were monitored by a differential dilatometer. They were heated at 10°C/min to a temperature between 1800°C and 2300°C and held at

Table 12: Powder descriptions of multiply-doped nano-powders

Sample Code	Description
PPG-125	0.1 wt% Al, 0.1 wt% Ti, 0.1 wt% W doped
PPG-126	0.5 wt% Al, 0.1 wt% Ti, 0.1 wt% W doped
PPG-127	1.0 wt% Al, 1.0 wt% Ti, 0.1 wt% W doped
PPG-128	1.0 wt% Al, 0.1 wt% Ti, 0.5 wt% W doped
PPG-129	0.1 wt% Al, 0.5 wt% Ti, 0.5 wt% W doped
PPG-130	0.5 wt% Al, 0.5 wt% Ti, 0.5 wt% W doped
PPG-131	1.0 wt% Al, 0.5 wt% Ti, 1.0 wt% W doped
PPG-132	0.1 wt% Al, 1.0 wt% Ti, 1.0 wt% W doped
PPG-133	0.5 wt% Al, 1.0 wt% Ti, 1.0 wt% W doped
PPG-134	0.1 wt% Al, 0.5 wt% Ti, 0.1 wt% W, 0.5 wt% Mg doped
PPG-135	1.0 wt% Al, 0.5 wt% Ti, 0.1 wt% W, 0.5 wt% Mg doped
PPG-136	0.5 wt% Al, 1.0 wt% Ti, 0.1 wt% W, 0.5 wt% Mg doped
PPG-137	0.5 wt% Al, 0.1 wt% Ti, 0.5 wt% wt% W, 0.5 wt% Mg doped
PPG-138	0.1 wt% Al, 1.0 wt% Ti, 0.1 wt% W, 0.5 wt% Mg doped
PPG-139	1.0 wt% Al, 1.0 wt% Ti, 0.5 wt% W, 0.5 wt% Mg doped
PPG-140	0.1 wt% Al, 0.1 wt% Ti, 1.0 wt% W, 0.5 wt% Mg doped
PPG-141	1.0 wt% Al, 0.1 wt% Ti, 1.0 wt% W, 0.5 wt% Mg doped
PPG-142	0.5 wt% Al, 0.5 wt% Ti, 1.0 wt% W, 0.5 wt% Mg doped

Table 13: Densities and weight losses of multiply-doped nano-powders

Sample number	Green density (%)	Archimedes density (%)	Weight loss (%)
PPG #125	68.73	90.69	3.91
PPG #126	69.36	90.42	6.05
PPG #127	70.61	88.02	6.97
PPG #128	69.04	89.38	7.60
PPG #129	69.74	89.18	5.52
PPG #130	72.98	92.42	8.10
PPG #131	71.10	93.23	7.55
PPG #132	72.03	94.11	9.41
PPG #133	71.07	93.84	6.33
PPG #134	66.98	95.42	4.68
PPG #135	65.95	92.65	7.90
PPG #136	66.51	91.06	6.61
PPG #137	67.25	92.09	6.28
PPG #138	66.26	93.89	4.49
PPG #139	66.62	91.42	8.20
PPG #140	68.23	94.19	4.98
PPG #141	67.53	91.31	8.35
PPG #142	65.60	89.31	5.60

that temperature for 1 h. The dimensional changes based on temperature are shown in Figure 18

The onset of sintering occurred at 1400°C, and nano-melting started at around 1900°C. During the nano-melting, the dimensional changes decelerated. At 2100°C dimensional changes re-accelerated, saturating at 2300°C. Two samples were heated to 1850°C and 1900°C with a constant heating rate of 10°C/min to avoid the nano-melting effect which starts around 1900°C. Samples showed a ∼5% net dimensional change. Previous work by Cho et al. concluded that the formation of a nano-sized liquid phase, which resulted from a decrease in the melting point due to a nano-size effect, coarsened the nano-particles and decreased the driving force for densification. The green and Archimedes densities and weight losses for all samples are shown in Table 16.

Based on the dilatometry traces and relative density data, the heating schedule was optimized. Two samples were heated to 1300°C at 50°C/min and held at that temperature for 2 h to remove residual B_2O_3. Temperature was then increased at 20°C/min to 2250°C or 2300°C and held for 1 h. Heating schedules were preformed under a He atmosphere. Dilatometry traces from the optimized heating schedules are shown in Figure 19. The green and Archimedes densities and weight losses of all samples are shown in Table 16.

4.3.3 Sintering of 44.46 mm disk

Four different powder treatments were used to prepare 44.46 mm diameter disks, as described in Table 17. The powders were uniaxially pressed (30 MPa) into cylindrical pellets ∼8 mm in height and 44.46 mm in diameter and then CIPed at 350 MPa.

All samples were heated to 1300°C at 50°C/min and held at that temperature for 2 h to remove residual B_2O_3. The temperature was then increased at 20°C/min to specific temperatures, which are described in Table 18, and held for 1 h. All heating

Table 14: Powder descriptions of PPG #163 - #168

Sample Code	Description
PPG-163	0.5 wt% Ti, 0.5 wt% Mg
PPG-164	0.1 wt% Al, 0.5 wt% Ti, 0.5 wt% Mg
PPG-165	0.5 wt% Ti, 0.1 wt% W, 0.5 wt% Mg
PPG-166	0.1 wt% Al, 0.5 wt% Ti, 0.1 wt% W, 0.5 wt% Mg (a repeat of PPG-134)
PPG-167	0.1 wt% Al, 0.5 wt% Ti, 0.1 wt% W, 1 wt% Mg
PPG-168	0.1 wt% Al, 0.5 wt% Ti, 0.1 wt% W, 0.5 wt% Mg (2% lubricant)

Table 15: Densities and weight losses of PPG #163- #168.

Sample number	Green density (%)	Archimedes density (%)	Weight loss (%)	Sample status
PPG #163	66.27	90.77	8.40	Cracked
PPG #164	67.78	94.34	5.90	Cracked
PPG #165	67.11	94.72	5.64	Crumbled
PPG #166	66.68	94.76	7.93	-
PPG #167	70.92	94.60	9.99	-
PPG #168	67.92	95.19	8.99	-

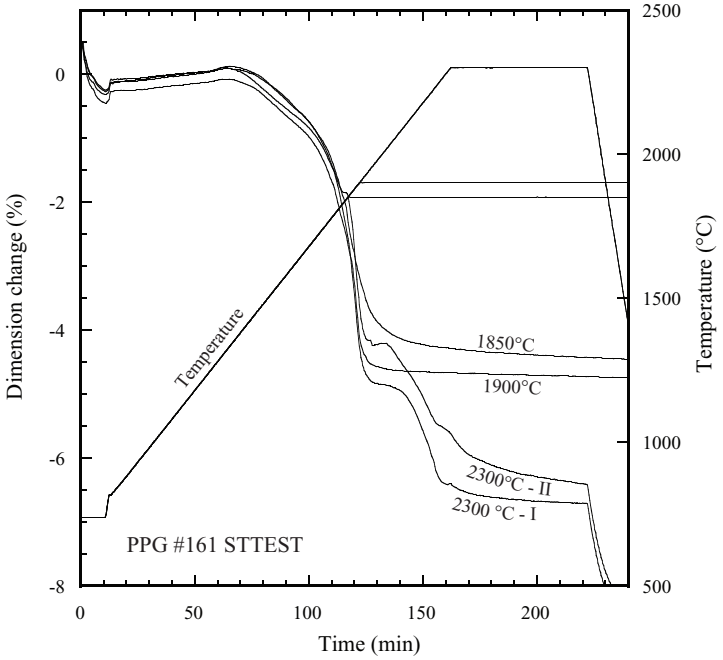

Figure 18: Dilatometric traces of PPG #166 at different sintering temperatures.

Table 16: Relative densities and weight losses of PPG #166 depending on sintering conditions.

Sample code	Green density (%)	Archimedes density (%)	Weight loss (%)	Sample status
2300°C - I	70.52	95.03	5.87	-
2300°C - II	70.46	95.10	6.03	-
1900°C	70.71	87.64	5.34	-
1850°C	71.46	86.42	4.98	-
2300°C	68.23	95.15	6.12	-
2250°C	72.38	95.01	6.20	-

Table 17: Descriptions of powder treatments used in green body processing.

Powder name	Description
AR	As received PPG #166 powder
WS	As received PPG #166 powder with stearic acid
MW-WS	Methanol washed PPG #166 powder with stearic acid
S325	sieved PPG #166 powder (S325)

schedules were preformed under a He atmosphere.

Except the sieved powder (S325), all samples showed surface defects with ∼70% green body densities after uniaxial pressing. After sintering at various temperatures, Archimedes densities increased to greater than ∼90% with defects. The photographs in Figure 20 show sintered disks as described in Table 18.

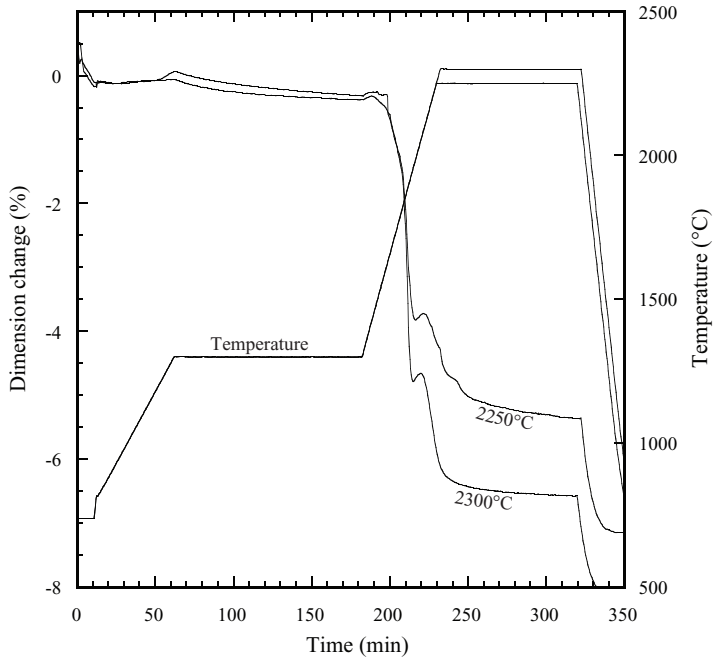

Figure 19: Dilatometric traces of PPG #166 at different sintering temperatures.

Table 18: Relative densities and weight losses of PPG #166. (AR: as received, WS: with stearic acid, MW-WS: methanol washing and with stearic acid, S325: sieved by 325 mesh)

Sample code	Green density (%)	Green body status	Archimedes density (%)	Weight loss (%)	Sample status
AR 2250°C	70.69	Surface defect	90.84	4.64	Cracked
AR 2300°C	70.74	Surface defect	90.78	4.94	Cracked
WS 2300°C	71.48	Surface defect	90.75	4.35	Cracked
WS 2330°C	70.76	Surface defect	91.00	4.28	Cracked
MW-WS 2330°C	70.92	Surface defect	-	-	Crumbled
MW-WS 2300°C	70.56	Surface defect	-	-	Crumbled
S325 2300°C	70.73	Good	92.81	4.19	Radial crack

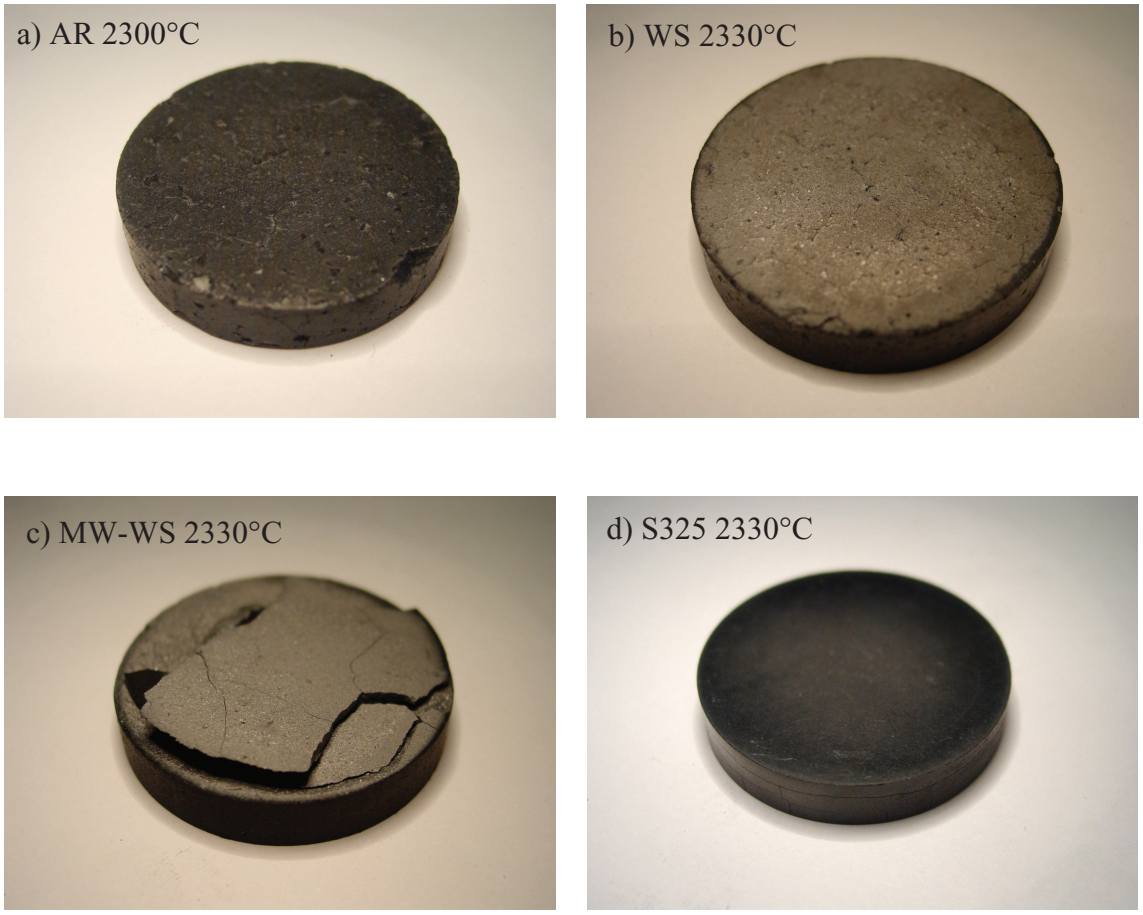

Figure 20: Photograph of 44.46 mm diameter disks sintered at 2300°C.

4.4 Encapsulated HIP

Encapsulated HIPing was preformed at temperatures below the nano-melting region in order to obtain a nano-sized grain structure. The green dimensional and Archimedes EHIPed densities and hardness values are shown in Table 19.

Table 19: Results of EHIPing of PPG #166 Nano-powder (All densities were calculated based on stoichiometric B_4C ($2.52 g/cm^3$)).

HIP temperature (°C)	Green relative density (%)	Archimedes relative density (%)	Hardness (kg/mm^2)
1850	61.9%	69.1%	-
1900	62.0%	96.2%	2347.4 ± 170.7

All green body densities were ∼62%. There was little improvement in relative density after EHIPing at 1850°C. After EHIPing at 1900°C, the relative density increased to 96.2%, and the hardness value was ∼2350 kg/mm^2.

The XRD results before and after EHIPing (Figure 21) show no unique phases relative to those observed after pressureless sintering. The graphite peaks showed some variation in their widths and scattering angles. The boron carbide peaks also showed some broadening relative to those after pressureless sintering.

Figure 22 shows regions of distinct phases at lower magnification (top). A bimodal distribution of grain sizes from ∼20 nm to ∼200 nm is observed at higher magnification (bottom).

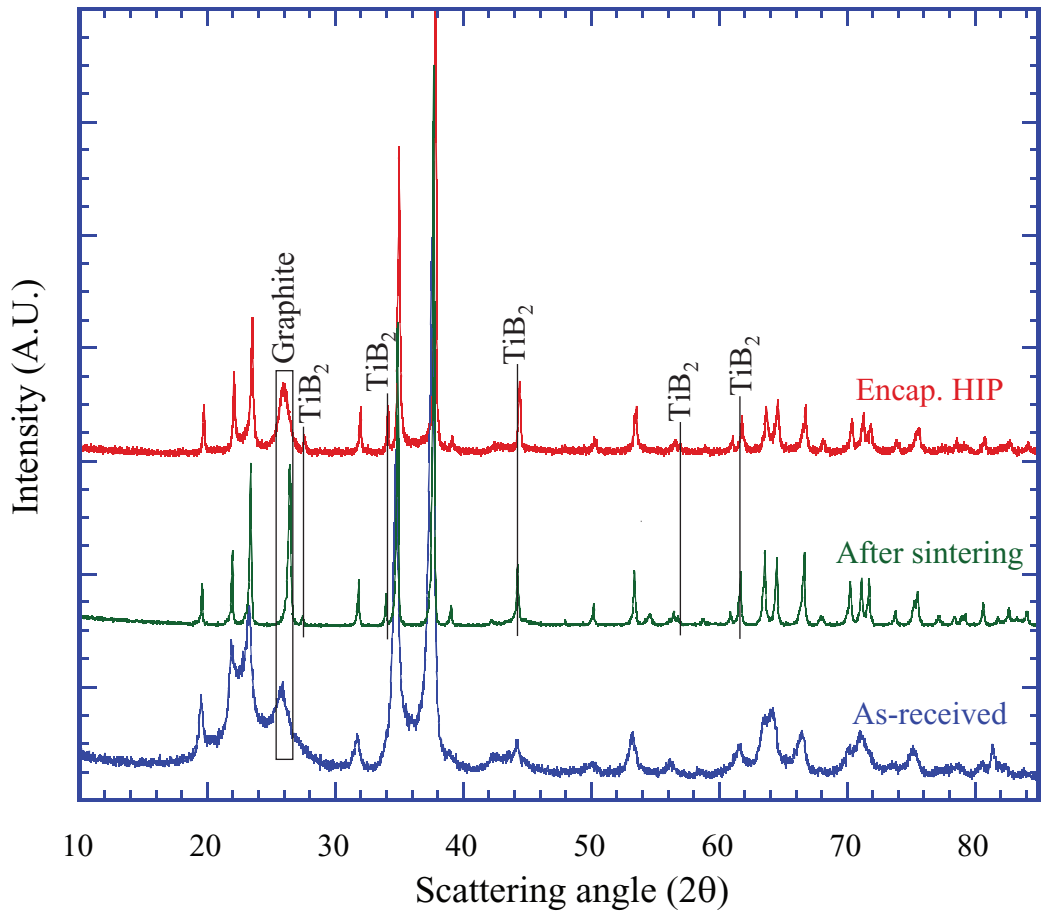

Figure 21: XRD peaks of powder #166 as-received, post-sintering, and post-EHIPing at 1900°C.

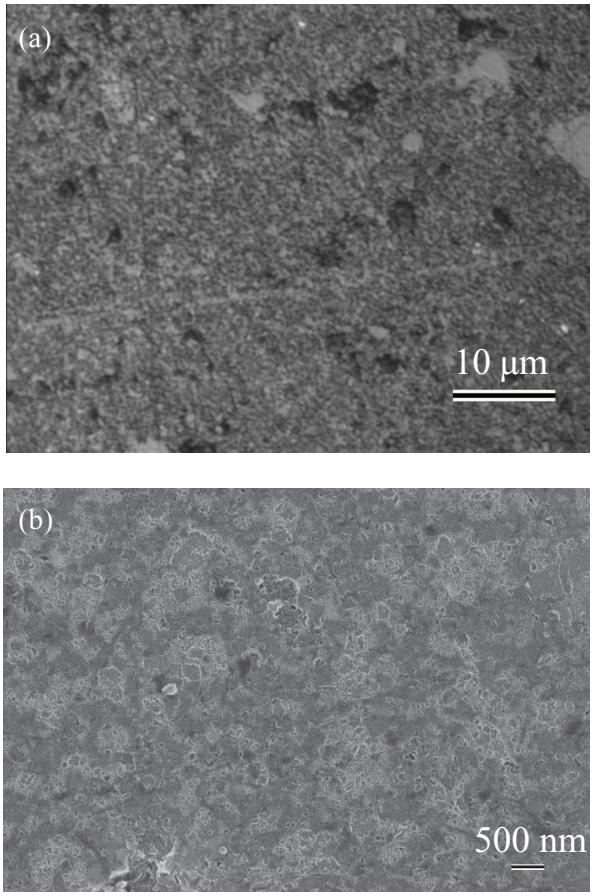

Figure 22: Microstructures of PPG nano-powder after EHIPing at 1900°C. a) Lower-magnification optical micrograph. b) Higher magnification SEM micrograph.

CHAPTER V

DISCUSSION

5.1 Powder study

Singly or multiply-doped powders were studied based on densities, phases before and after sintering, and hardness values. Phase identification using X-ray diffraction showed that all nano-powders were mainly B_4C with graphite and other compounds, related to dopants, as secondary phases. All dopants can be classified into three different categories. The first type of dopants, including Fe and Al, did not form any secondary phases. Y and Mg were of the second type of dopants that tended to form oxides. The last type of dopants, such as Ti, Zr, Nb and W, formed borides. All as-received nano-powders showed a line broadening due to their small size. Secondary phases were detected using XRD data. Peak heights varied depending on the dopant concentrations. Peak heights of graphite increased in the case of Y-doped powders, but the opposite trend was observed for Nb-doped and B-rich, Al-doped nano-powders. The changes in the peak heights depended on the reactions between the dopants and B_4C. The crystallinity of the powders varied in the cases of Al-doped and La-doped powders.

Dilatometry traces of all nano-sized powders showed two-stage sintering, which is typically observed in nano-powders. Cho et. al observed that solid-state sintering occurs after volatilization of B_2O_3 at $\sim$1300°C; small humps in the dilatometric traces support this conclusion [9]. After initial sintering, a plateau was observed, and shrinkage slowed, stopped, or reversed due to the coarsening of nano-particles.

It was observed that the species and concentration of the dopant shifted the onset temperature for sintering as well as nano-melting. The sintering onset temperatures

for Al-doped powders shifted to higher temperatures as the concentration of Al increased; however, the onset of nano-melting did not change. Additionally, the slopes during nano-melting and net dimensional changes tended to increase as the concentration of Al increased. For Y-doped powders, there was a slight change in sintering onset temperature, while the nano-melting regions shifted to lower temperature as concentration increased. Powders doped with boride formers such as La and Nb showed slight changes in their sintering onset temperatures and nano-melting region characteristics. The observed shift in the onset of nano-melting temperature is considered to be due to variations in particle size. Smaller particles are believed to nano-melt at lower temperature due to their larger surface area to volume ratio. The XRD data for sintered Nb-doped powders showed sharp peaks compared with those of the as-received powders, which implies that the grain size is on the order of a micron primarily due to the coarsening mechanism of nano-melting.

5.2 Post-HIPing

Singly-doped samples which obtained densities greater than 93% of their theoretical density after pressureless sintering in experiments prior to this study were post-HIPed. Post-HIPing significantly improved both densities and hardness values. XRD data shows that there were changes in some of the phases during post-HIPing. These phase changes indicate reactions between dopants and the B_4C phase. These reactions differed depending on the dopants. All samples undergoing post-HIPing were doped with boride-forming dopants during powder synthesis. However, XRD data for the Zr-doped sample showed a decrease in the peak heights of the ZrB_2 phase, while ZrC was detected as a new phase. These results imply that the formation of ZrC is a preferred reaction under post-HIPing conditions. The W-doped sample showed a different trend. The change in peak height in WB_2 and W_2B_5 indicated that the more boron rich phase (W_2B_5) was the preferred phase under HIPing conditions.

The microstructure of post-HIPed samples shows distribution of secondary phases and pores. The Al-doped sample showed a homogeneous distribution of B_4C and graphite phases with a grain size of less than 10 μm, with some abnormally grown grains. Both the Zr-doped and Ti-doped samples showed relatively large grains with secondary phases, such as TiB_2 and ZrB_2, at grain boundaries. All TiB_2 and ZrB_2 was observed at grain boundaries. The microstructure of the Zr-doped sample showed characteristics of liquid phase sintering, such as a rounded grain shape and an irregular shape to the ZrB_2 phase at grain boundaries. The ZrB_2 phase formed a liquid phase during sintering which stimulated grain growth of the B_4C phase, creating a courser microstructure. The W-doped sample showed large distinct graphite regions separate from the B_4C phase as shown in Figure 16.

The densities and hardness values before and after HIPing are summarized in Table 23. The hardness values increased due to a strong correlation between hardness and porosity, which decreases with increasing density. The standard deviations of the hardness values increased as dopant concentration increased due to the presence of large grains and secondary phases.

5.3 Optimization for Scaling-Up

Powder compositions, heating schedules, and green processing techniques were investigated for scaling up. Only multiply-doped powders were investigated for optimization. Based on single-dopant powders, combinations of Al, Ti, W, and Mg were tested. These powders showed improved final densities and acceptable weight losses which are shown in Table 13 and Table 15.

A heating schedule was optimized based on the dilatometry traces shown in Figure 18. Multiply-doped powders showed a double-stage sintering behavior, which is typically observed in nano-sized powder. Sintering below the onset of the nano-melting temperature was attempted in order to obtain a nano-sized grain structure

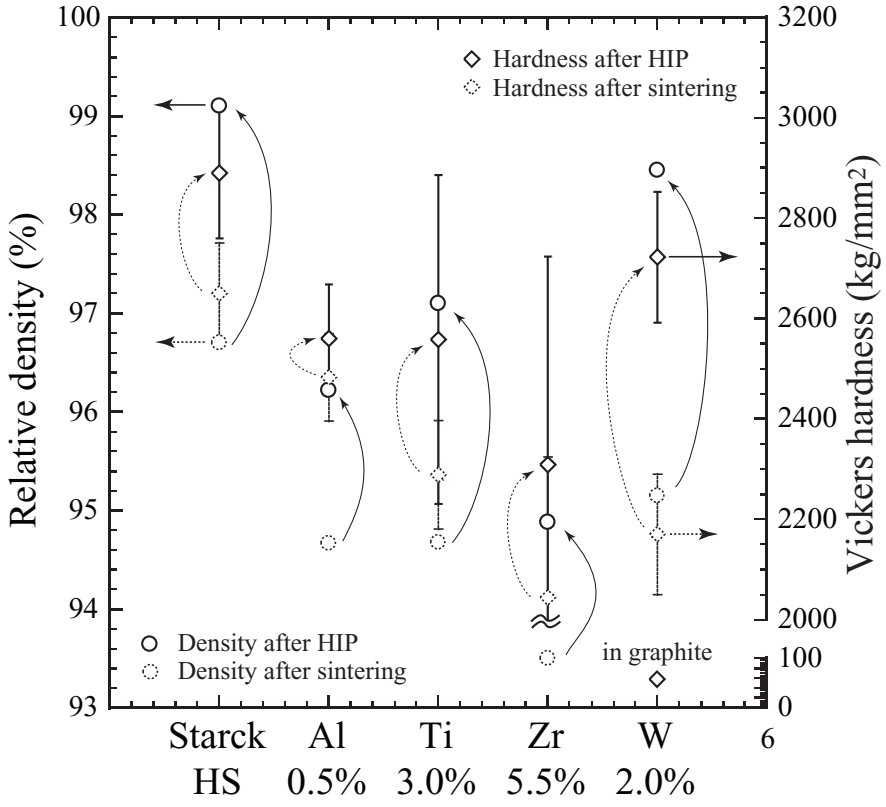

Figure 23: Hardness and density changes based on dopant before and after HIPing.

by avoiding the coarsening of the nano-powder. The dilatometric traces showed that dimensional changes in the samples sintered at 1850°C and 1900°C did not proceed beyond the nano-melting region. The densities of these samples were less than 90%. However, samples sintered at 2300°C showed ∼95% densities with ∼6% weight losses. The soak at 1300°C for 2 h was introduced to remove residual B_2O_3 phase. Two different sintering temperatures were investigated, although there was little difference between the final densities shown in Table 16.

Sintering of the 44.46 mm diameter disks was performed based on the optimized composition and heating schedule. Nano-powders treated in four different ways, as described in Table 17, had different visible characteristics, as shown in Figure 20. Sintered bodies from the as-received (AR) powder and powder with steric acid (WS) showed critical surface defects, such as large surface cracks and pores. The sintered body prepared with steric acid after methanol washing (MW-WS) cracked during sintering. These defects are believed to originate from impurities such as residual glass phases and non-uniform packing during pressing. The sample formed from powder sieved with a 325 mesh grid showed the best results, though the presence of small radial cracks was not eliminated. This is believed to be an effect of nano-melting.

5.4 Encapsulated HIP

Encapsulated HIPing under nano-melting temperature was preformed in order to obtain a fully densified B_4C sample with a nano-sized grain structure. The sample EHIPed at 1900°C showed a 96.2% Archimedes density and a hardness value of ∼2350 Kg/mm^2. The XRD results before and after EHIPing show no phase changes relative to those observed during normal pressureless sintering at temperatures over 2000°C. The graphite peaks show some variation in their widths and scattering angles; this is considered to be a nano-size effect. The boron carbide peaks also showed some broadening relative to those obtained after pressureless sintering. Micrographs at

lower magnifications show regions of distinct phases. At higher magnification, a bimodal distribution of grain sizes ranging from 20 nm to 200 nm is observed. The cause for the bimodal distribution is considered to be related to the nano-melting effect observed in pressureless sintering.

The fine grain size obtained after EHIP was never observed after pressureless sintering, resulting in the same relative densities. However, the hardness value obtained was comparable to pressurelessly sintered samples of the same relative density. The possible positive effects of the nano-sized grain structure are believed to be attenuated by the domination of porosity and second phases on the measured hardness values.

CHAPTER VI

CONCLUSION

Based on the data obtained during the sintering of singly-doped boron carbide nano-powders, four dopants have been determined to have desirable effects on the sintering behaviors of nano-powders. The four dopants are Al, Ti, Zr, and W. After doping, Y acts as an oxide former, while Nb and La form boride compounds. Nano-powders doped with boride formers show greater relative densities after sintering when compared to oxide forming compounds. A composition was selected which can be sintered to ∼95% theoretical density with minimal weight loss. The post-HIPing process improved relative densities as well as the measured Vicker's hardness values.

Scaling up the sintering process with this nano-powder will require more work in order to eliminate the small surface cracks observed in the 44.46 mm diameter samples. Powder processing such as methanol washing and sieving increases the quality of green bodies, which reduces defects in the sintered bodies. Properly processed samples of composition #166 show a hardness value of ∼2600 Kg/mm^2 and minimal surface defects. B_4C nano-powder may soon be an industrially feasible raw material for fabricating dense parts.

Due to the nano-melting phenomenon observed by differential dilatometry, a nano-sized grain structure cannot be achieved by pressureless sintering followed by post-HIPing. As an alternative method, EHIPing yields a more nano-crystalline structure. The sample of composition #166 had a measured Vickers hardness value of ∼2350 Kg/mm^2; the sample does not show properties expected of a nano-sized grain structure. The low measured Vickers hardness value is likely due to the presence of secondary phases such as graphite and borides. Future work using EHIP should focus

on studing temperature and pressure for EHIPing in order to create a fully densified B_4C nano-crystalline structure, as well as the elimination of secondary phases.

REFERENCES

[1] J. Shackelford and W. Alexander, *CRC Materials Science and Engineering Handbook*. Boco Raton: CRC Press (1991).

[2] F. Thevenot, "Boron carbide - a Comprehensive review," *Journal of the European Ceramic Society*, **6** [4] 205-225 (1990).

[3] T. Vasilos and S. K. Dutta, "Low temperature hot pressing of boron carbide and its properties," *American Ceramic Society Bulletin*, **53** [5] 453-54 (1984).

[4] R. Vaban and D. Stover, "Processing and properties of nanophase non-oxide ceramics," *Materials Science and Engineering A*, **301** [3] 215-220 (1988).

[5] R. Rice, "Effects of environment and temperature on ceramic tensile strength-grain size relations," *Journal of Materials Science*, **32** 3071-87 (1997).

[6] Y. Kanno, K. kawase and K. Nakano, "Additive effect on sintering of boron carbide," *Journal of the Ceramic Society of Japan*, **95** [11] 1137-40 (1987).

[7] K. Schwetz, "Boron carbide, boron nitride, and metal boride," *Ullmann's Encyclopedia of Industrial Chemistry, Sixth Edition*, Wiley-VCH Verlag GmpH (1999).

[8] N. Cho, Z. Bao and R. F. Speyer, "Density- and hardness-optimized pressureless sintered and post-hot isostatic pressed B_4C," *Journal of Materials Research*, **20** [8] 2110-16 (2005).

[9] N. Cho, K. Silver, Y. Berta, R. F. Speyer, N. Varnier and C. H. Hung, "Densification of carbon-rich boron carbide nanopowder compacts," *Journal of Materials Research*, **22** [5] 1354-59 (2007).

[10] R. R. Ridgway, "Boron carbide. a new crystalline abrasive and wear-ressisting product," *Electrochemical Society - Transactions*, **66** 117-133 (1934).

[11] D. Emin, "Structure and single phase regime of boron carbides," *Physical Review B*, **38** 6041-55 (1998).

[12] H. Pierson, *Handbook of Refractory Carbides and Nitrides: Properties, Characteristics, Processing and Applications,* Noyes Publishing, Westwood, NJ (1996).

[13] J. S. Reed *Principles of Ceramic Processing,* 2nd Ed., John Wiley and Sons, New York (1995).

[14] R. Angers and M. Beauvy, "Hot pressing of boron carbide," *Ceramic International*, **10** [2] 49-55 (1984).

[15] H. Kim, Y. Young and H. E. Kim, "Densification and mechanical properties of B_4C with Al_2O_3 as a sintering aid," *Journal of the American Ceramic Society*, **83** [11] 2863-5 (2000).

[16] V. Skorokhod, Jr., M. D. Vlajic and V. D. Krstic, "Mechanical properties of pressureless sintered boron carbide containing TiB_2 phase," *Journal of Materials Science Letters*, **15** [15] 1337-39 (1996).

[17] Z. Zakhariev and D. Radev, "Properties of polycrystalline boron carbide sintered in the presence of W_2B_5 without pressing," *Journal of Materials Science Letters*, **7** [7] 695-96 (1988).

[18] K. Schwetz and G. Vogt, "Process for the production of dense sintered articles of boron carbide," *U.S. Patent*, no. 4,195,066 (1980).

[19] K. Schwetz, W. Grellner and A. Lipp, "Mechanical properties of hip treated sintered boron carbide," *Institute of Physics Conference Series*, [75] 413-426 (1986).

[20] H. Lee and R. F. Speyer, "Pressureless sintering of boron carbide," *Journal of the American Ceramics Society*, **86** [9] 1468-73 (2003).

[21] O. Vasylkiv, Y. Sakka and V. V. Skorokhod, "Low-temperature processing and mechanical properties of zirconia and zirconia-alumina nanoceramics," *Journal of The American Ceramic Society*, **86** [2] 299-304 (2003).

[22] J. Groza and R. Dowding, "Nanoparticulate materials densification," *Nanostructured Materials*, **7** [7] 749-768 (1996).

[23] R. Vaben and D. Stover, "Processing and properties of nanophase ceramics," *Journal of Materials Processing Technology*, **92** 77-84 (1999).

[24] Hans T. Larker, "Hot isostatic pressing," *ASM Publication Ceramics&Glasses*, **4** 194-201 (1991).